

# Multiple Cations Nanoconfinement in Ultrathin $V_2O_5$ Nanosheets Enables Ultrafast Ion Diffusion Kinetics Toward High-performance Zinc Ion Battery

Yang Liu, Chengjie Lu, Yunting Yang, Wenshu Chen, Fei Ye, Hongliang Dong, Yuping Wu, Renzhi Ma, and Linfeng Hu\*

Nanoconfinement of cations in layered oxide cathode is an important approach to realize advanced zinc ion storage performance. However, thus far, the conventional hydrothermal/solvothermal route for this nanoconfinement has been restricted to its uncontrollable phase structure and the difficulty on the multiple cation co-confinement simultaneously. Herein, this work reports a general, supramolecular self-assembly of ultrathin  $V_2O_5$  nanosheets using various unitary cations including  $Na^+$ ,  $K^+$ ,  $Mg^{2+}$ ,  $Ca^{2+}$ ,  $Zn^{2+}$ ,  $Al^{3+}$ ,  $NH_4^+$ , and multiple cations ( $NH_4^+ + Na^+$ ,  $NH_4^+ + Na^+ + Ca^{2+}$ ,  $NH_4^+ + Na^+ + Ca^{2+} + Mg^{2+}$ ). The unitary cation confinement results in a remarkable increase in the specific capacity and Zn-ion diffusion kinetics, and the multiple cation confinement gives rise to superior structural and cycling stability by multiple cation synergetic pillaring effect. The optimized diffusion coefficient of Zn-ion ( $7.5 \times 10^{-8} \text{ cm}^2 \text{ s}^{-1}$ ) in this assembly series surpasses most of the V-based cathodes reported up to date. The work develops a novel multiple-cations nanoconfinement strategy toward high-performance cathode for aqueous battery. It also provides new insights into the guest cation regulation of zinc-ion diffusion kinetics through a general, supramolecular assembly pathway.

rechargeable battery systems beyond lithium-ion batteries.<sup>[1,2]</sup> Among them, aqueous zinc-ion batteries (AZIBs) are gaining considerable attention.<sup>[3–5]</sup> As the next generation of large-scale energy storage units due to their advantages in high theoretical capacity ( $820 \text{ mAh g}^{-1}$  and  $5854 \text{ mAh cm}^{-3}$ ; low redox potential ( $-0.763 \text{ V}$  versus standard hydrogen electrode); high safety and low cost.<sup>[6–8]</sup> During the past few years, great progress has been made to demonstrate a lot of novel AZIBs cathode materials including inorganic Mn, V, Mo-based oxides/sulfides, and metal-organic compounds of Prussian blue analogues (PBAs).<sup>[9–15]</sup> Among them, manganese-based materials suffer from  $Mn^{2+}$  dissolution caused by the Jahn–Teller effect and also the fast fade of capacities.<sup>[16–18]</sup> Prussian blue analogues always deliver inferior specific capacity ( $<60 \text{ mAh g}^{-1}$ ) and low voltage plateau ( $0.7 \text{ V}$  versus  $Zn/Zn^{2+}$ ).<sup>[19–21]</sup> Vanadium-based compounds are very promising and received

## 1. Introduction

The rapid development of grid-scale energy storage and flexible electronics has triggered tremendous demands in advanced

extensive attention owing to their remarkable advantage on specific capacity.<sup>[3,22–24]</sup>


Especially, recent progress revealed that a cation nanoconfinement strategy in vanadium oxides can significantly improve its electrochemical properties due to the as-embedded metallic cations acting as pillars in the layered frameworks and expanding the interlayer spacing to facilitate Zn ion diffusion. For example, Zhou et al. synthesized  $Li_xV_2O_5 \cdot nH_2O$  nanosheets cathode by a hydrothermal treatment of  $V_2O_5$  and  $LiNO_3$  solution with the assistance of  $H_2O_2$ .<sup>[25]</sup> Alshareef disclosed that  $Ca_{0.24}V_2O_5 \cdot 0.83H_2O$  nanobelts, prepared through a hydrothermal process of  $CaCl_2$  and  $V_2O_5$  mixed solution.<sup>[26]</sup> Although the hydrothermal/solvothermal route can synthesize a series of  $M_xV_2O_5 \cdot nH_2O$  ( $M = Li, Ca, Zn, Na, Mn, Co, Cu, Zn, Al, Cr, Ag, \text{etc.}$ ),<sup>[27]</sup> these  $M_xV_2O_5 \cdot nH_2O$  derivatives generally cannot be crystallized in the same phase structure. Furthermore, it is also impossible to embed multiple cations simultaneously in the host through the hydrothermal/solvothermal route, making the difficulty on material design, property optimization, and understanding on host–guest interlayer chemistry. Accordingly, developing a general strategy for cation nanoconfinement strategy is essential but still very challenging.

Y. Liu, C. Lu, Y. Yang, W. Chen, F. Ye, L. Hu  
 School of Materials Science and Engineering  
 Southeast University  
 Nanjing 211189, P. R. China  
 E-mail: [linfenghu@seu.edu.cn](mailto:linfenghu@seu.edu.cn)

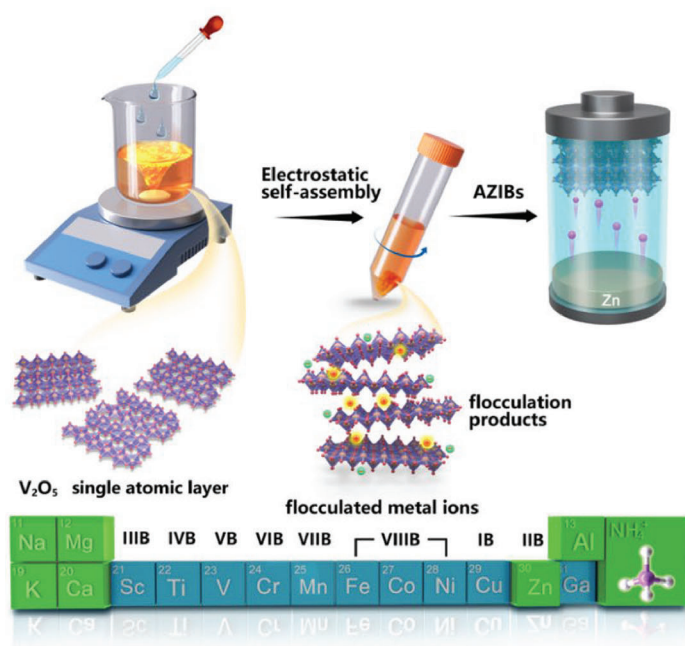
H. Dong  
 Center for High Pressure Science and Technology Advanced Research  
 Shanghai 201203, P. R. China

Y. Wu  
 School of Energy and Environment  
 Southeast University  
 Nanjing 211189, P. R. China

R. Ma  
 Research Center for Materials Nanoarchitectonics  
 National Institute for Materials Science (NIMS)  
 Namiki 1-1, Tsukuba, Ibaraki 305-0044, Japan

 The ORCID identification number(s) for the author(s) of this article can be found under <https://doi.org/10.1002/adma.202312982>

DOI: 10.1002/adma.202312982



**Scheme 1.** Schematic illustration for the supramolecular self-assembly strategy.

Layered materials have been well recognized in electrochemical energy storage owing to its rich intercalation chemistry and very high active surface.<sup>[28–31]</sup> More importantly, two-dimensional (2D) nanosheets with single-layer to multiple-layer thickness obtained from their layered bulk precursor can be regarded as inorganic supermolecules.<sup>[32]</sup> As soon as adding some oppositely charged ions or molecules into this 2D nanosheet colloidal system, re-stacking of the nanosheets driven by electrostatic interaction occurs immediately to form some flocculent precipitate, which can be easily recovered by filtration or low-speed centrifugation.<sup>[30–32]</sup>

Inspired by this phenomenon, we consider it is possible to realize a general strategy for cation nanoconfinement in the layered  $V_2O_5$  host for superior zinc ion storage. Herein, we reported a general supramolecular self-assembly of ultrathin  $V_2O_5$  nanosheets induced by various metallic and nonmetallic cations (**Scheme 1**). A series of  $M_xV_2O_5 \cdot nH_2O$  ( $M = NH_4^+, Li^+, Na^+, K^+, Mg^{2+}, Ca^{2+}, Zn^{2+}, Al^{3+}$ ) can be easily synthesized by this strategy. More interestingly, we can realize a simultaneously cooperative confinement of several cations ( $NH_4^+/Na^+$ ,  $NH_4^+/Na^+/Ca^{2+}$ ,  $NH_4^+/Na^+/Ca^{2+}/Mg^{2+}$ ) by this strategy. We make a systematic comparison on the  $Zn^{2+}$  storage capacity, long-term cycling stability, and  $Zn^{2+}$  diffusion kinetics on this self-assemble series. The unitary cation confinement results in superior storage capacity and very fast  $Zn$ -ion diffusion kinetics. The optimized diffusion coefficient of zinc ion ( $7.5 \times 10^{-8} \text{ cm}^2 \text{ s}^{-1}$ ) in this assembly series surpasses most of the V-based cathodes reported up to date. Density functional theoretical (DFT) simulation further reveals a declined  $Zn$ -ion diffusion barrier by unitary cation nanoconfinement due to a significantly weakened interaction between  $Zn^{2+}$  and dangling oxygen atom of  $V_2O_5$ . The multiple cation confinement gives rise to an enhancement on the long-term cyclability and structural stability by multiple cation synergetic pillaring effect.

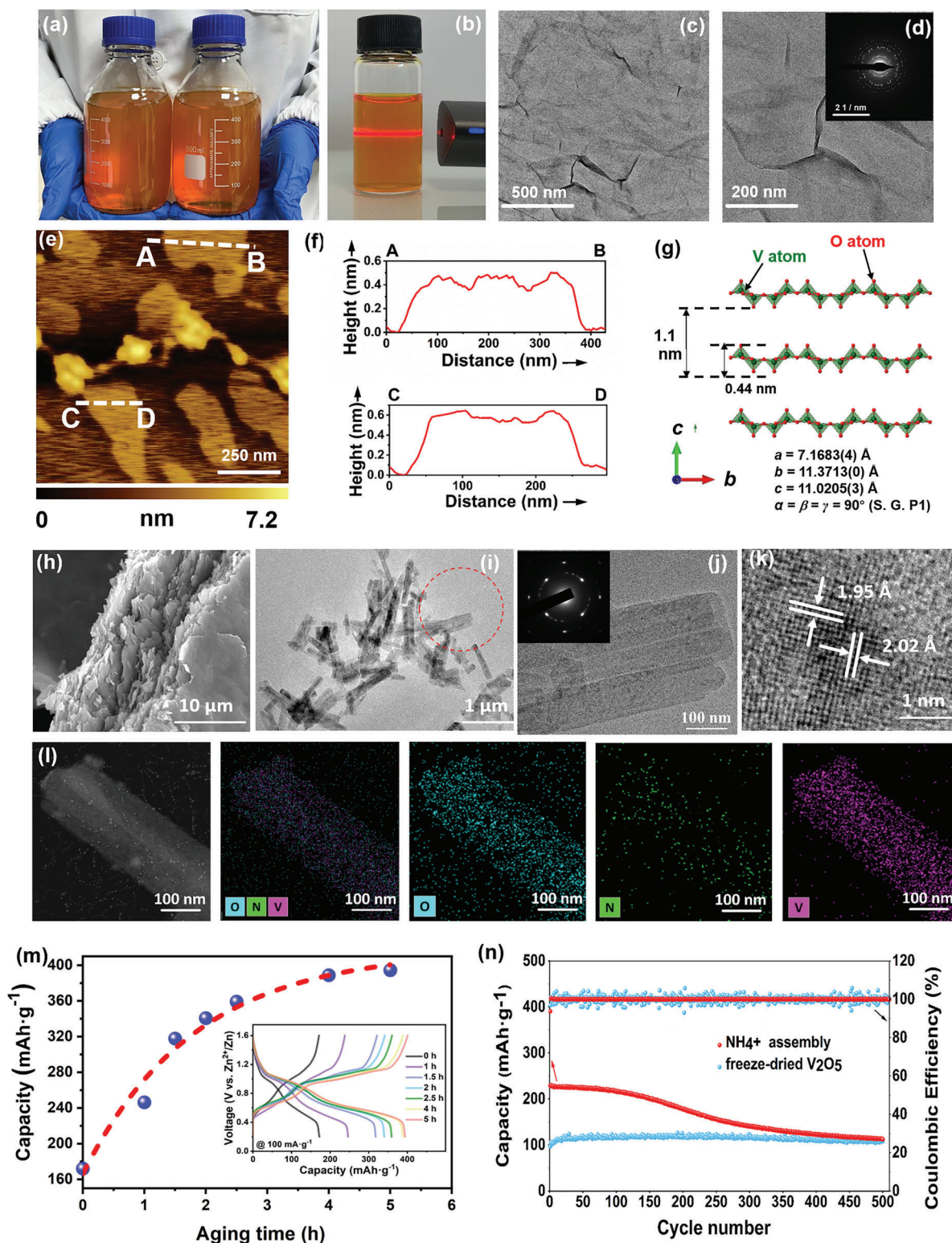
- ✓ **Unitary assembly:**  
 $NH_4^+, Na^+, K^+, Mg^{2+}, Ca^{2+}, Zn^{2+}, Al^{3+}$
- ✓ **Binary assembly:**  
 $NH_4^+ + Na^+$
- ✓ **Ternary assembly:**  
 $NH_4^+ + Na^+ + Ca^{2+}$
- ✓ **Quarternary assembly:**  
 $NH_4^+ + Na^+ + Ca^{2+} + Mg^{2+}$
- $NH_4^+ + Na^+ + Ca^{2+} + Mg^{2+} + \dots$

## 2. Results and Discussion

### 2.1. Supramolecular Assembly of $NH_4^+$

$V_2O_5$  colloid suspension was prepared by a simple hydrothermal method reported previously.<sup>[33]</sup> One liter of aqueous colloid with a clear Tyndall light scattering can be produced (**Figure 1a,b**). Transmission electron microscopy (TEM) observation further reveals numerous thin sheet-like objects with a lateral size of 200–300 nm and wrinkled edges (**Figure 1c,d**). The corresponding selected area electron diffraction (SAED) pattern (**Figure 1d**) presents typical polycrystalline rings due to the overlap of these nanosheets. Atomic force microscopy (AFM) characterization also detects 2D ultrathin sheets with a lateral dimension in the range of 300–400 nm (**Figure 1e**). The height profile in **Figure 1f** demonstrates a thickness of 0.40–0.53 nm, which is very close to the crystallographic thickness (0.44 nm) of  $V_2O_5$  single atomic layer (**Figure 1g**). Known that most of the unilamellar oxide nanosheets can be regarded as a kind of Bronsted acid group, which can adsorb positive charged species.<sup>[34]</sup> Herein, the average zeta potential of the resulting  $V_2O_5$  colloid suspension is determined as  $-60.4 \text{ mV}$ , suggesting the possibility of colloidal self-assembly by some positively charged ions.

Then we first selected  $NH_4^+$  as the anti-cation to verify the self-assembly behavior. Flocculation phenomenon immediately occurred by mixing the colloidal suspension with 0.2 M  $NH_4Cl$  aqueous solution to form apparent needle-like precipitation at the bottom of the colloidal suspension, and the orange colloid gradually transformed into colorless transparent. After the flocculation, the product was aged for several hours in this solution with continuous magnetic stirring to tune its zinc ion storage capacity as discussed below. X-ray diffraction (XRD) patterns of the flocculation product after aging are given in **Figure S1a** (Supporting Information). The sharp peaks around 5–9° can be indexed



as (001) basal series, of which the d-spacing can be regarded as the basal spacing of the re-stacked structure. Note that some out-plane ( $hkl$ ,  $l \neq 0$ ) diffraction peaks can also be detected in both freeze-dried  $V_2O_5$  powder and the  $NH_4^+$  flocculation product, demonstrating that the yield of the single-layer  $V_2O_5$  nanosheets cannot reach up to 100% with the presence of some multilayered structure in the as-prepared  $V_2O_5$  nanosheets.<sup>[30,35]</sup> Compared to the freeze-dried sample obtained from the  $V_2O_5$  colloid suspension, the 00 $l$  ( $l = 1, 2, 3, 4, 5, 6$ ) characteristic peaks exhibit a shift toward larger diffraction angle for our  $NH_4^+$  flocculation product, indicating the slight decrease in the basal spacing from 11.6 to 11.1 Å due to the host-guest interaction between  $NH_4^+$  and the  $V_2O_5$  single layer.<sup>[36]</sup> The thermogravimetric analysis (TGA) of the as-prepared sample measured in the temperature range of 25–600 °C was carried out (Figure S1b, Supporting Information). The weight loss below 50 °C (domain I) is ascribed to the removal of absorbed water, and the loss between 50 °C and 145 °C (domain II) should be assigned to the evaporation of the crystal water. Moreover, the loss after 145 °C (domain III) could be ascribed to the evaporation of the intercalated  $NH_4^+$  cations,<sup>[37,38]</sup> which was further confirmed by the XRD pattern of the  $NH_4^+$  flocculation sample after 400 °C (Figure S1c, Supporting Information). Thus, the chemical formula of as-prepared flocculation product can be identified as  $(NH_4)_{0.77}V_2O_5 \cdot 0.8H_2O$ . Scanning electron microscopy (SEM) observation of the self-assembled sample reveals large-sized agglomerations with lateral size up to several micrometers due to the stacking of  $V_2O_5$  nanosheets (Figure 1h). Transmission electron microscope (TEM) images (Figure 1i,j) show 2D nanoribbon morphology, suggesting the nanosheets might be drastically fractured into nanoribbons during the restacking. High-resolution transmission electron microscopy (HRTEM) images taken from the nanoribbon surface in Figure 1k exhibited a clear 2D lattice fringe, and the 0.202, 0.195 nm spacing of which agrees well with the expected separation of (006), (120) planes of layered  $V_2O_5$ , respectively. Energy dispersive spectrum (EDS) mapping (Figure 1l) reflects the uniform distribution of V and O elements in the sample, and the appearance of N element distribution confirms the successful  $NH_4^+$  embedding in the layered  $V_2O_5 \cdot nH_2O$  host.

Subsequently, the zinc-ion battery performance was investigated in CR-2032 coin cells using a Zn foil anode, 2.0 M Zn(OTf)<sub>2</sub> electrolyte, and a glass fiber separator. Interestingly, we found the specific capacity is highly dependent on the aging time after the self-assembly process. As shown in Figure 1m, the  $(NH_4)_{0.77}V_2O_5 \cdot 0.8H_2O$  sample aged at 1, 1.5, 2, 2.5, 4, and 5 h exhibits a discharge capacity of 246.3, 317.8, 340.7, 359.2, 388.8, and 394.5 mA h g<sup>-1</sup> at 100 mA g<sup>-1</sup>, respectively (Figure 1m). Further increase in the aging time leads to the saturated capacity at this threshold time. Ultimately, the specific capacity ( $C$ ) versus aging time ( $t$ ) can be fitted as an exponential growth tendency as follows:

$$C = -250e^{-0.55t} + 417 \quad (1)$$

The phase evolution of this self-assembled sample during the aging process was identified by XRD patterns (Figure S2, Supporting Information). For the fresh flocculation sample without any aging treatment, the presence of asymmetric diffraction peaks at 47.2°, 50.8°, and 60.5° with a tail toward a higher angu-

lar side is a typical characteristic of a disordered lamellar structure. According to the previous study,<sup>[30]</sup> the  $V_2O_5$  single-layer nanosheets were restacked with well maintaining the in-plane atomic arrangement but losing its regular sheet-stacking sequence. However, these asymmetric diffraction peaks converted into symmetrical after 1–5 h aging, indicating such a disordered lamellar structure may recrystallize into a 3D ordered crystal. Careful SEM observation indicates that the surface of the sample aging at 1 h exhibits restacked sheet morphology with a very smooth surface (Figure S3, Supporting Information). With prolonging the aging time, the surface generally converted to rather rough and porous, which should be responsible for the as-observed capacity increase in Figure 1m. Cyclic voltammetry (CV) curves with varied scan rates give a vital dependence of the peak current density and scan rate to clarify the capacity contribution type for Zn-ion storage (Figure S4, Supporting Information).<sup>[39,40]</sup> The capacitive contribution can be calculated as 59.3%, 67.6%, 75.0%, 81.0%, 86.3%, and 91.0% at the scan rate of 0.1, 0.2, 0.4, 0.6, 0.8, and 1.0 mV s<sup>-1</sup>, respectively. Ex situ XRD characterization identifies a typical Zn<sup>2+</sup> intercalation/de-intercalation mechanism of our  $(NH_4)_{0.77}V_2O_5 \cdot 0.8H_2O$  sample the same as the most V-based cathodes reported previously (Figure S5, Supporting Information). Figure S6 (Supporting Information) gives the rate performance of  $(NH_4)_{0.77}V_2O_5 \cdot 0.8H_2O$  electrode with the average capacities of 366.2, 290.6, 244.1, 204.2177.5, and 165.4 mAh g<sup>-1</sup> at the current densities of 0.05, 0.1, 0.2, 0.5, 0.8, and 1.0 A g<sup>-1</sup>, respectively. When the current density was reset to 0.05 A g<sup>-1</sup>, a recovered capacity of 363.2 mA h g<sup>-1</sup> was achieved. The long-term cyclability of our as-assembled  $(NH_4)_{0.77}V_2O_5 \cdot 0.8H_2O$  sample is depicted in Figure 1n. Although the cycle stability decreases after  $NH_4^+$  nanoconfining, its initial capacity is remarkably higher than that of the bare  $V_2O_5$  freeze-dried sample.

## 2.2. Extend to Other Guest Cations

We found our supramolecular colloidal self-assembly strategy can be easily extended to other guest cations such as Li<sup>+</sup>, Na<sup>+</sup>, K<sup>+</sup>, Mg<sup>2+</sup>, Ca<sup>2+</sup>, Zn<sup>2+</sup>, and Al<sup>3+</sup>. Needle-like precipitation can be clearly observed except the case of Li<sup>+</sup> which exhibits very fine sediment hardly been recovered by filtration or high-speed centrifugation (Figure 2a). In the case of Li<sup>+</sup> assembly, any sediment cannot be observed and the TEM image (Figure S7, Supporting Information) shows no apparent morphology differences compared with the original nanosheet. We consider that the Li<sup>+</sup> might not make the re-stacking of  $V_2O_5$  nanosheets through electrostatic force due to the relatively smaller surface charged density of Li<sup>+</sup> compared with other cations (Mg<sup>2+</sup>, Ca<sup>2+</sup>, Zn<sup>2+</sup>, Al<sup>3+</sup>). SEM observation (Figure S8, Supporting Information) revealed that all samples consisted of large agglomerations due to the stacking of  $V_2O_5$  nanosheets. The chemical formula of these samples flocculated by Na<sup>+</sup>, K<sup>+</sup>, Mg<sup>2+</sup>, Ca<sup>2+</sup>, Zn<sup>2+</sup>, and Al<sup>3+</sup> was determined by inductive coupled plasma (ICP) (Supplementary Tab S1) and TGA analysis (Figure S9, Supporting Information), which can be identified as Na<sub>0.34</sub>V<sub>2</sub>O<sub>5</sub>·0.46H<sub>2</sub>O, K<sub>0.30</sub>V<sub>2</sub>O<sub>5</sub>·0.16H<sub>2</sub>O, Mg<sub>0.16</sub>V<sub>2</sub>O<sub>5</sub>·0.82H<sub>2</sub>O, Ca<sub>0.14</sub>V<sub>2</sub>O<sub>5</sub>·0.72H<sub>2</sub>O, Zn<sub>0.29</sub>V<sub>2</sub>O<sub>5</sub>·0.83H<sub>2</sub>O, and Al<sub>0.19</sub>V<sub>2</sub>O<sub>5</sub>·1.19H<sub>2</sub>O, respectively. The comparison of the corresponding XRD patterns (Figure S10, Supporting Information) illustrates its d-spacing

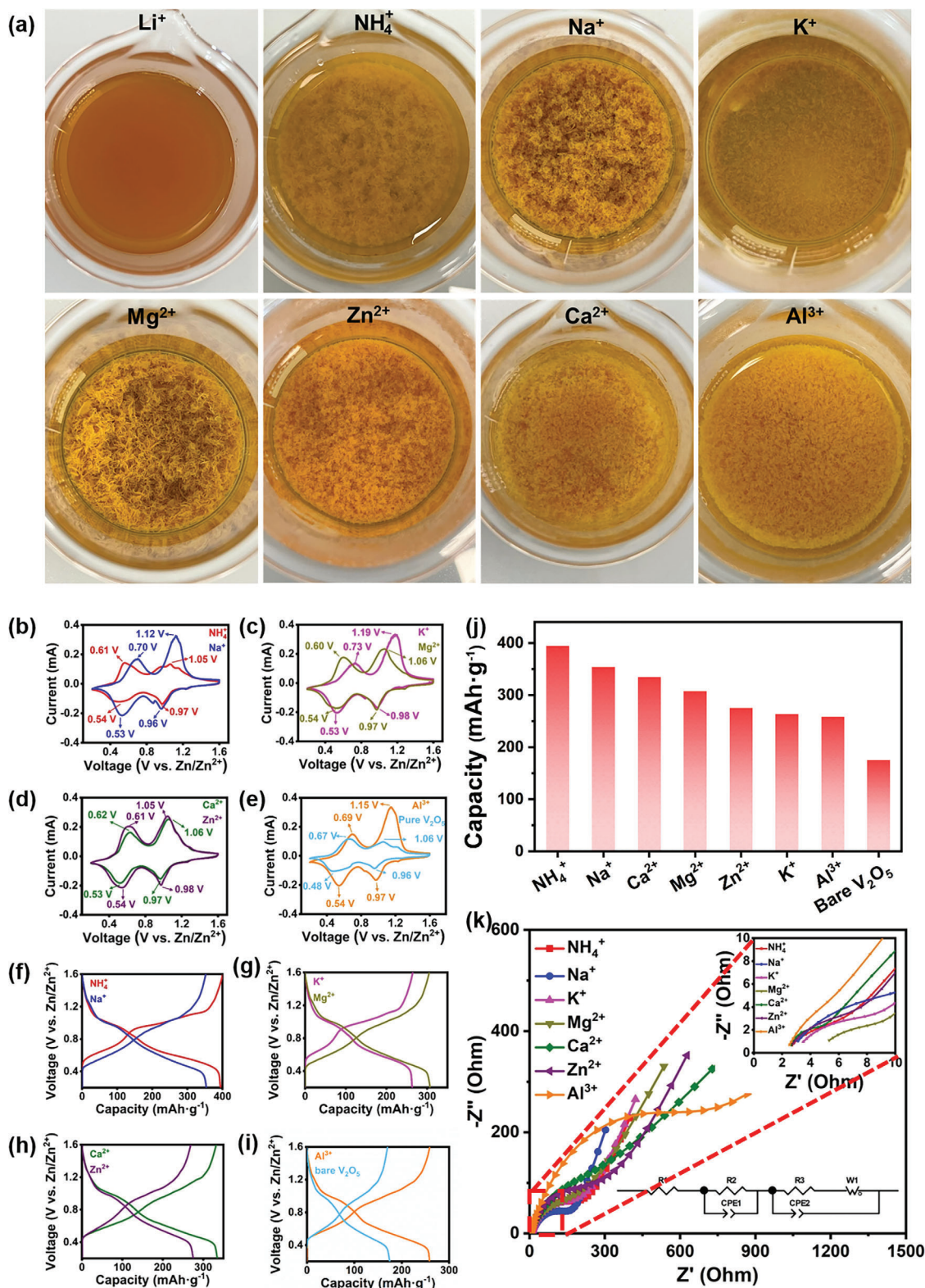


**Figure 2.** a) Optical images of the  $\text{Li}^+$ ,  $\text{NH}_4^+$ ,  $\text{Na}^+$ ,  $\text{K}^+$ ,  $\text{Mg}^{2+}$ ,  $\text{Ca}^{2+}$ ,  $\text{Zn}^{2+}$ ,  $\text{Al}^{3+}$ -based  $\text{M}_x\text{V}_2\text{O}_5\cdot n\text{H}_2\text{O}$  flocculation products. b–e) Cyclic voltammetry (CV) profiles and f–i) the corresponding galvanostatic charge-discharge (GCD) profiles of  $\text{Na}^+$ ,  $\text{K}^+$ ,  $\text{Mg}^{2+}$ ,  $\text{Ca}^{2+}$ ,  $\text{Zn}^{2+}$ ,  $\text{Al}^{3+}$ -based  $\text{M}_x\text{V}_2\text{O}_5\cdot n\text{H}_2\text{O}$  and bare  $\text{V}_2\text{O}_5$  sample at  $0.05\text{ A g}^{-1}$ , respectively. j) Comparison of the discharge specific capacity of  $\text{M}_x\text{V}_2\text{O}_5\cdot n\text{H}_2\text{O}$  in the first charge–discharge cycle at  $0.05\text{ A g}^{-1}$ . k) Electrochemical impedance spectroscopy (EIS) spectrum of  $\text{M}_x\text{V}_2\text{O}_5\cdot n\text{H}_2\text{O}$  with the enlarged image in high frequency region inserted, showing a depressive trend of  $R_{\text{ct}}$  with  $\text{Al}^{3+}$  ( $642\ \Omega$ ) >  $\text{Ca}^{2+}$  ( $200\ \Omega$ ) >  $\text{Na}^+$  ( $135.4\ \Omega$ ) >  $\text{NH}_4^+$  ( $134\ \Omega$ ) >  $\text{Zn}^{2+}$  ( $120.1\ \Omega$ ) >  $\text{K}^+$  ( $111.6\ \Omega$ ) >  $\text{Mg}^{2+}$  ( $38.85\ \Omega$ ).

of  $\text{Al}_{0.19}\text{V}_2\text{O}_5 \cdot 1.19\text{H}_2\text{O}$  (14.1 Å) >  $\text{Ca}_{0.14}\text{V}_2\text{O}_5 \cdot 0.72\text{H}_2\text{O}$  (13.4 Å) >  $\text{Mg}_{0.16}\text{V}_2\text{O}_5 \cdot 0.82\text{H}_2\text{O}$  (13.3 Å) >  $\text{Zn}_{0.29}\text{V}_2\text{O}_5 \cdot 0.83\text{H}_2\text{O}$  (13.0 Å) >  $\text{Na}_{0.34}\text{V}_2\text{O}_5 \cdot 0.46\text{H}_2\text{O}$ , and  $\text{K}_{0.30}\text{V}_2\text{O}_5 \cdot 0.16\text{H}_2\text{O}$  (11.2 Å) >  $(\text{NH}_4)_{0.77}\text{V}_2\text{O}_5 \cdot 0.8\text{H}_2\text{O}$  (11.1 Å). Considering the ionic radii order of these metallic ions is:  $r(\text{Al}^{3+}, 50 \text{ pm}) < r(\text{Mg}^{2+}, 65 \text{ pm}) < r(\text{Zn}^{2+}, 74 \text{ pm}) < r(\text{Na}^+, 95 \text{ pm}) < r(\text{Ca}^{2+}, 99 \text{ pm}) < r(\text{K}^+, 133 \text{ pm}) < r(\text{NH}_4^+, 143 \text{ pm})$ ,<sup>[41–45]</sup> it is unexpected that smaller ion radius result in a larger interlayer spacing in the  $\text{M}_x\text{V}_2\text{O}_5 \cdot n\text{H}_2\text{O}$  series in principle. Based on the TGA analysis, we hypothesize this phenomenon might be attributed to the discrepancy on hydrated state of different guest cations. This hypothesis was confirmed by the FTIR and Raman spectra (Figures S11 and S12, Supporting Information). One can see the  $\text{Mg}^{2+}$ ,  $\text{Ca}^{2+}$ ,  $\text{Zn}^{2+}$ ,  $\text{Al}^{3+}$ -based samples deliver a much stronger peak at 1614  $\text{cm}^{-1}$  assigned to bending vibration peak of the interlayer water than that of bare  $\text{V}_2\text{O}_5$  nanosheets prepared by freeze-drying. In contrast, such a bending vibration enhancement on  $\text{Na}^+$ ,  $\text{K}^+$ , and  $\text{NH}_4^+$ -based  $\text{M}_x\text{V}_2\text{O}_5$  is not very apparent. This result suggests that the as-confined  $\text{Mg}^{2+}$ ,  $\text{Ca}^{2+}$ ,  $\text{Zn}^{2+}$ , and  $\text{Al}^{3+}$  in  $\text{V}_2\text{O}_5$  interlayer by our supramolecular self-assembly is highly hydrated. Meanwhile, the other one ( $\text{Na}^+$ ,  $\text{K}^+$ , and  $\text{NH}_4^+$ ) is confined as a low hydration state, leading to a relatively smaller d-spacing.

The zinc-ion storage behavior of this  $\text{M}_x\text{V}_2\text{O}_5 \cdot n\text{H}_2\text{O}$  ( $\text{M} = \text{Na}^+$ ,  $\text{K}^+$ ,  $\text{Mg}^{2+}$ ,  $\text{Ca}^{2+}$ ,  $\text{Zn}^{2+}$ ,  $\text{Al}^{3+}$ ) series was first studied using CV at 0.1  $\text{mV s}^{-1}$ . As shown in Figure 2b–e, all samples exhibit a very analogous shape with a pair of redox peaks located at 0.9–1.2 and 0.4–0.8 V, respectively. Galvanostatic charge-discharge (GCD) profiles at 100  $\text{mA g}^{-1}$  were well consistent with the CV curves (Figure 2f–i). Figure 2j summarizes the specific zinc ion storage capacities of all  $\text{M}_x\text{V}_2\text{O}_5 \cdot n\text{H}_2\text{O}$  cathodes in the first cycle, showing a trend with  $\text{NH}_4^+$ -based  $\text{M}_x\text{V}_2\text{O}_5 \cdot n\text{H}_2\text{O}$  (394.5  $\text{mAh g}^{-1}$ ) >  $\text{Na}^+$  (353.8  $\text{mAh g}^{-1}$ ) >  $\text{Ca}^{2+}$  (334.8  $\text{mAh g}^{-1}$ ) >  $\text{Mg}^{2+}$  (307.1  $\text{mAh g}^{-1}$ ) >  $\text{Zn}^{2+}$  (275.2  $\text{mAh g}^{-1}$ ) >  $\text{K}^+$  (263.1  $\text{mAh g}^{-1}$ ) >  $\text{Al}^{3+}$  (258.6  $\text{mAh g}^{-1}$ ). It is worth noting that the bare  $\text{V}_2\text{O}_5$  nanosheet sample just delivers a much smaller capacity of 180  $\text{mAh g}^{-1}$ , demonstrating the significant enhancement of zinc ion storage capacity through our supramolecular assembly. XPS spectra identify a reversible  $\text{V}^{5+} \leftrightarrow \text{V}^{4+}/\text{V}^{3+}$  transformation during  $\text{Zn}^{2+}$  insertion and extraction in this  $\text{M}_x\text{V}_2\text{O}_5 \cdot n\text{H}_2\text{O}$  series (Figure S13, Supporting Information). Electrochemical impedance spectroscopy (EIS) was then performed to investigate the electrochemical kinetics. The corresponding results are collected in Figure 2k, which delivers a semicircle in the high-frequency region and a line in the low-frequency region. After fitting,  $\text{Mg}^{2+}$ -based  $\text{M}_x\text{V}_2\text{O}_5 \cdot n\text{H}_2\text{O}$  cathode exhibited the smallest charge transfer resistance ( $R_{\text{ct}}$ ) of 38.85 Ω while  $\text{Al}^{3+}$ -based  $\text{M}_x\text{V}_2\text{O}_5 \cdot n\text{H}_2\text{O}$  delivered the highest  $R_{\text{ct}}$  of 642 Ω (Figure 2k). We further verify the regulation of electronic conductivity using density of states (DOS) by DFT calculations with a case study of  $\text{K}^+$  nanoconfinement. Apparent states of electron density can be found at the Fermi level after cation nanoconfinement, which can be mainly attributed to the shift of Fermi surface toward a high-energy level (Figure S14, Supporting Information). As a result, the electronic conductivity of the nanoconfinement sample is deduced to be better than that of pristine  $\text{V}_2\text{O}_5$ , which is well consistent with the as-achieved  $R_{\text{ct}}$  results. The rate-capability and long-term cycle performance of  $\text{Na}^+$ ,  $\text{K}^+$ ,  $\text{Mg}^{2+}$ ,  $\text{Ca}^{2+}$ ,  $\text{Zn}^{2+}$ ,  $\text{Al}^{3+}$  nanoconfinement sample is given in Figures S15 and S16 (Supporting Information). All of

these assembled series deliver superior rate-performance and cycling capacity to that of the bare  $\text{V}_2\text{O}_5$  freeze-dried sample.

### 2.3. Multiple Guest Cations Cooperative Assembly

Interestingly, we found it possible to realize multiple cations confinement in this  $\text{V}_2\text{O}_5$  host using our self-assembly strategy. When two, three even four kinds of cations sources were simultaneously introduced in the  $\text{V}_2\text{O}_5$  nanosheet colloid, similar flocculation phenomenon was observed. The corresponding XRD patterns in Figure 3a deliver no significant discrepancy between these unitary, binary, ternary, and quaternary self-assembled series except a shift in the (001) peaks, suggesting the successful confinement of multiple cations. The basal spacing gradually increased from an initial 11.1 Å ( $\text{NH}_4^+$ ) up to 11.4 Å ( $\text{Na}^+ + \text{NH}_4^+$ ), 13.6 Å ( $\text{Na}^+ + \text{NH}_4^+ + \text{Ca}^{2+}$ ), and then showed a slight decrease to 13.4 Å for quaternary  $\text{Na}^+ + \text{NH}_4^+ + \text{Ca}^{2+} + \text{Mg}^{2+}$  confinement. The detailed chemical molar ratio of the various metal cations in the product by ICP atomic emission spectroscopy is listed in Table S2 (Supporting Information). TEM observation and EDS mapping also confirm the success of this multiple guest cations cooperative self-assembly (Figure 3b–d). All of the samples show a lamellar stacking morphology, and the corresponding EDS mapping verifies the uniform distribution of Na, N, Ca, and Mg elements in the samples. Strikingly, our self-assembly process shows the advantage compared with the conventional hydrothermal method, which hardly realizes the simultaneous embedding of several cations. When four cations of  $\text{NH}_4^+$ ,  $\text{Na}^+$ ,  $\text{Mg}^{2+}$ , and  $\text{Ca}^{2+}$  were introduced into the hydrothermal system, the corresponding XRD pattern confirms the product is a mixture of  $\text{VO}_2 \cdot n\text{H}_2\text{O}$  and  $\text{CaV}_8\text{O}_{20} \cdot n\text{H}_2\text{O}$  (Figure S17, Supporting Information).

The success of simultaneous co-assembly of multiple cations in  $\text{V}_2\text{O}_5$  host endows the opportunity to compare the interlayer cation-dependent performance accurately and to deeply understand the host–guest interlayer chemistry. GCD profiles in Figure S18a (Supporting Information) show the specific capacity of our self-assembly series and bare  $\text{V}_2\text{O}_5$  nanosheets. All of the self-assembled samples in this series exhibit a high capacity outperforming that of the bare  $\text{V}_2\text{O}_5$  nanosheets. On the other hand, with the introduction of more intercalated cations, the capacity gradually decreases from initial 394.5 to 284.6  $\text{mAh g}^{-1}$ . Such a result can be understood by the degressive tendency on specific capacity after unitary  $\text{NH}_4^+$ ,  $\text{Na}^+$ ,  $\text{Ca}^{2+}$ , and  $\text{Mg}^{2+}$  confinement (Figure S18b, Supporting Information).

In situ Raman characterization was then employed to investigate the energy storage mechanism of the as-assembled quaternary sample ( $\text{Na}^+ + \text{NH}_4^+ + \text{Ca}^{2+} + \text{Mg}^{2+}$ ) as cathodes, which was depicted in a 2D contour image accompanied by the corresponding GCD profile in Figure 3e. Notably, the peak at 150  $\text{cm}^{-1}$  attributed to the V–O–V bond slightly shifts to a higher wavenumber and then back to the normal position during discharge/charge processes (see black arrow), indicating that the V–O–V bond was first strengthened by  $\text{Zn}^{2+}$  adsorption/insertion, then weakened by  $\text{Zn}^{2+}$  extraction during the charge process. Overall, within the  $\text{Zn}^{2+}$  insertion in the discharge process, the Raman peaks gradually decreased, demonstrating that the adsorption and insertion of Zn ions break the bonds between

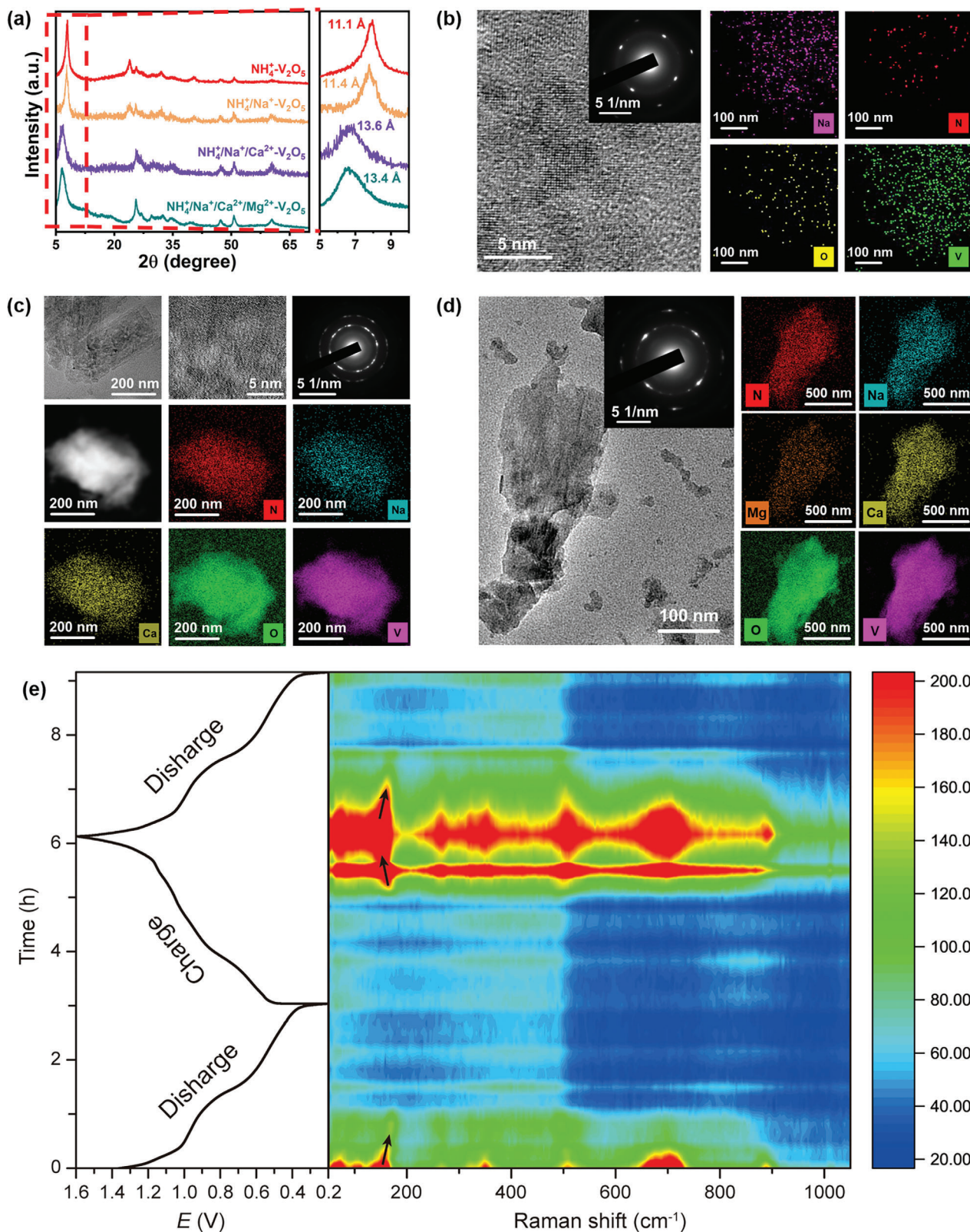


**Figure 3.** a) X-ray diffraction (XRD) patterns of the  $\text{NH}_4^+$ ,  $\text{NH}_4^+ + \text{Na}^+$ ,  $\text{NH}_4^+ + \text{Na}^+ + \text{Ca}^{2+}$ ,  $\text{NH}_4^+ + \text{Na}^+ + \text{Ca}^{2+} + \text{Mg}^{2+}$  cooperative self-assembly products, respectively. High-resolution transmission electron microscopy (HRTEM) image and energy dispersive spectrum (EDS) mapping images of b)  $\text{NH}_4^+ + \text{Na}^+$ , c)  $\text{NH}_4^+ + \text{Na}^+ + \text{Ca}^{2+}$ , d)  $\text{NH}_4^+ + \text{Na}^+ + \text{Ca}^{2+} + \text{Mg}^{2+}$  system. e) In situ Raman contour image of our quaternary  $\text{NH}_4^+ + \text{Na}^+ + \text{Ca}^{2+} + \text{Mg}^{2+}$  assembled sample during the first discharge/charge/discharge processes (at  $0.05\text{ A g}^{-1}$ ).

V and O atoms inside the cathode crystals. With the potential increasing to 1.6 V, those Raman signals were recovered due to the extraction of Zn ions, demonstrating the good reversibility of our quaternary self-assembled  $V_2O_5$  materials for aqueous Zn ion storage.

Impressively, we found the multiple cations confinement in this  $V_2O_5$  host gives rise to the enhancement on the cycling stability (Figure 4a). With the increase in the category of intercalated guest cations, the multiple cations confinement sample shows a superior long-term stability with a higher capacity retention. The corresponding capacity retention after 1000 cycles of the  $NH_4^+ + Na^+$ ,  $NH_4^+ + Na^+ + Ca^{2+}$  and  $NH_4^+ + Na^+ + Ca^{2+} + Mg^{2+}$  cooperative self-assembly products is 37.9%, 80.2%, and 88.4%, respectively. Previous work by other groups has revealed that introducing guest species (e.g., metal ions, water molecules, organic molecules, and organometallic molecules) into vanadium-based materials is favorable to relieving the structural deterioration derived from the pillar effect, stabilizing the host structure upon cycling and enlarge the crystal tunnel for more cation occupation.<sup>[46]</sup> In our case, the improvement in cyclability by multiple cations confinement should be attributed to the increase in the d-spacing and structural stability by multiple cation synergistic pillaring effect.<sup>[41–45]</sup>

DFT calculations were carried out to give a deep understanding on the multiple cation synergistic pillaring effect. Figure 4b shows the atomic configuration of the layered  $V_2O_5$  host with an interlayer distance of 11.6 Å set according to the corresponding XRD characterization in Figure S1 (Supporting Information). Two types of oxygen atoms can be observed in this  $V_2O_5$  structure respectively: the dangling oxygen ( $O^D$ ) labeled in green and the bonding oxygen ( $O^B$ ) labeled in blue. Accordingly, there are two void spaces showing different storage capacities while holding ions or molecules: one is a small void (SV space) surrounded by  $O^D$  atoms with a radius around 1.5 Å, and another is a large void (LV space) beneath  $O^B$  atoms with a radius above 4.0 Å. It is interesting to find that the  $O^D$  atoms shift slightly toward the as-intercalated  $Na^+$  and  $K^+$  due to the large ionic radius of  $Na^+$ ,  $K^+$ , and the long-range affinity effect (depicted in Figure 4b). Figure 4c compares the energy discrepancy while forming  $M-O^B$  and  $M-O^D$  bonds ( $M = Na^+$ ,  $K^+$ ,  $Mg^{2+}$ ,  $Ca^{2+}$ ,  $Zn^{2+}$ ,  $Al^{3+}$ ). It can be seen that  $Al^{3+}$  and  $Zn^{2+}$  are energetically favorable for intercalation in the small empty space surrounded by  $O^D$  (achieving their maximum formation energy  $\Delta E_{MO^D}$  of  $-5.98$  and  $-1.72$  eV, respectively), while the others including  $Na^+$ ,  $K^+$ , and  $Ca^{2+}$  are much more favorable to stay in the large empty space forming  $M-O^B$  bonds (achieving their maximum formation energy  $\Delta E_{MO^B}$  of  $-3.53$ ,  $-3.71$ , and  $-4.86$  eV, respectively). By counting the bond length of  $M-O^B/M-O^D$  in the optimized  $M_xV_2O_5$  structure, the intercalation site of the confined cation is highly dependent on its ionic radius or hydrated ionic radius (Figure 4d). More importantly, the intercalation results given in Figure 4e demonstrated that the energetically preferred accommodation site on the  $V_2O_5$  host for various cations is quite different, accordingly, the increase of intercalated cation species from binary to quaternary guest cations, or even more, can provide a multiple cation synergistic pillaring effect with various cations at different accommodation sites. These multiple guest cations located at different accommodation sites are favorable for a much more stable structure during the zinc-ion insertion and extraction process.

## 2.4. Zinc Ion Diffusion Kinetic Regulation

We further identified the zinc ion diffusion kinetic of this self-assembly series through the galvanostatic intermittent titration technique (GITT) measurement (Figure 5a,b, Figure S19, Supporting Information). Among these samples,  $K^+$ -based  $M_xV_2O_5 \cdot nH_2O$  exhibited the highest  $Zn^{2+}$  diffusion coefficient of  $7.5 \times 10^{-8} \text{ cm}^2 \text{ s}^{-1}$  (platform within 0.9–1.2 V) and  $2.5 \times 10^{-8} \text{ cm}^2 \text{ s}^{-1}$  (platform within 0.4–0.8 V). Figure 5c shows the comparison of  $Zn^{2+}$  diffusion coefficient in this series with a degenerative trend that  $D_{K^+} > D_{Na^+} > D_{NH_4^+} > D_{Ca^{2+}} > D_{Al^{3+}} > D_{Mg^{2+}} > D_{Zn^{2+}} > D_{\text{bare } V_2O_5} > D_{\text{binary}} > D_{\text{ternary}} > D_{\text{quaternary}}$ . This result indicates that the nanoconfinement of one kind of cation in layered  $V_2O_5$  is beneficial to accelerate zinc-ion transport kinetic. However, further increase of interlayer cations gives rise to the negative influence on the zinc-ion transport. Strikingly, all of the  $Zn^{2+}$  diffusion coefficient kinetic in our assembly products is significantly superior to that of  $M_xV_mO_n$  based cathode materials reported recently by the conventional hydrothermal route.<sup>[23–25,43,47–52]</sup> This result identifies that the cation nanoconfinement by this self-assembly strategy would significantly facilitate the rapid transport of zinc ion and result in the larger diffusion coefficient of zinc ion.

The effect of intercalation cation species on the  $Zn^{2+}$  diffusion kinetics was further identified in our DFT theoretical simulation. Considering that  $Mg^{2+}$ ,  $Al^{3+}$ , and  $Ca^{2+}$  were characterized to be in a high hydrated state for this nanoconfinement and the fundamental role of interlayer water in charge storage for  $V_2O_5$  bilayers has been revealed by Lu et al. recently,<sup>[53]</sup> herein we carried out qualitative discussion on this kinetics effect by selecting  $Na^+$  and  $K^+$ -based samples with a much low hydrated state. Figure 5d shows the as-calculated  $Zn^{2+}$  diffusion barrier on the pure  $V_2O_5$  single atomic layer without any cation confinement. Surprisingly, a high energy barrier of 1.02 eV was found in this case, indicating a poor mobility of  $Zn^{2+}$  in  $V_2O_5$  accompanied by the strong interaction between  $Zn^{2+}$  and surrounding  $O^D$  atoms. In contrast, the presence of  $H_2O$  or  $NH_4^+$  in the LV space was found to be remarkably favorable for the diffusion behavior, with the barrier declining to 0.87 and 0.64 eV for  $V_2O_5 \cdot H_2O$  and  $V_2O_5 \cdot NH_4^+$ , respectively. Figure 5e further illustrates the charge difference density map of  $K_xV_2O_5$  with Zn ion located at energetically minimum site during its diffusion. It can be apparently seen in Figure S20 (Supporting Information) that dangling oxygen atoms shift with the presence of  $K^+$  confinement in layered  $V_2O_5$ , leading to a weakened hampering effect of Zn ion diffusion by surrounding oxygen atoms. As a result, the distance between each two  $O^D$  atoms was prolonged, and the shape of diffusion barrier curve based on the calculated diffusion pathway depicts the maximum energy in the middle of two  $O^D$  atoms (red line in Figure 5f), which is remarkably different from that of pure  $V_2O_5$  (Figure 5d). Correspondingly, an obvious reduction in the diffusion energy barrier was observed from initial 1.02 eV (pristine  $V_2O_5$ ) to 0.89 eV ( $Na_xV_2O_5$ ) and 0.78 eV ( $K_xV_2O_5$ ), which contributes to the enhanced  $Zn^{2+}$  diffusion kinetics by  $Na^+$ ,  $K^+$  confinement.

Another question is why the  $Zn^{2+}$  diffusion kinetics gradually degenerated with the introduction of two or more cations in the  $V_2O_5$  host. The influence of binary cations nanoconfinement was studied by stacking  $Na^+$  and  $K^+$  in one large void space. As confirmed in Figure 5f, such a binary  $Na^+/K^+$  stacking yields a high



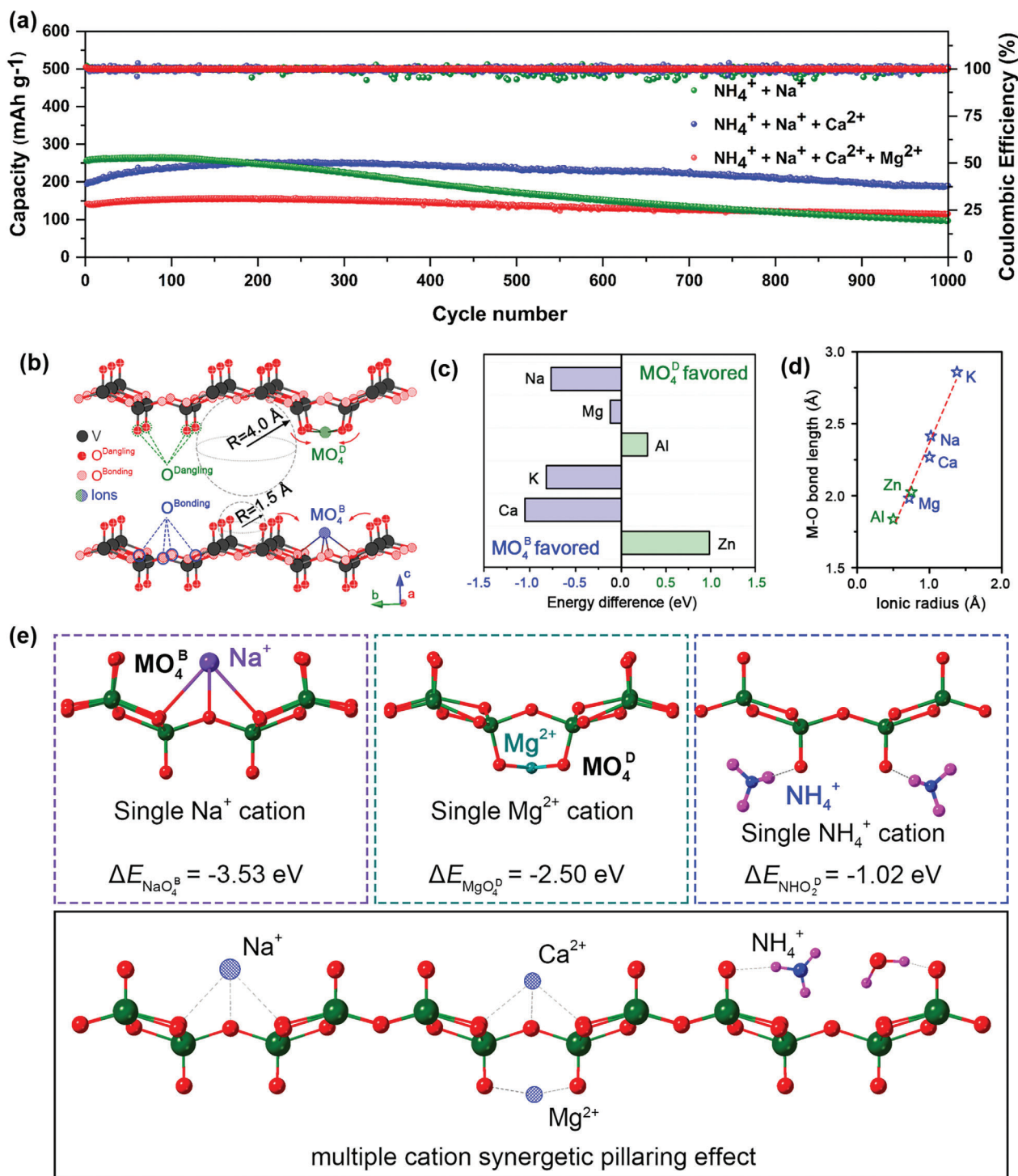


**Figure 4.** a) Long-term cycle performance of the cooperative self-assembly products at  $0.2 \text{ A g}^{-1}$ . b) Atomic scheme of  $\text{V}_2\text{O}_5$  showing two types of oxygen atoms, the  $\text{O}^{\text{Bonding}}$  (labeled by  $\text{O}^{\text{B}}$  in blue) in lattice, and  $\text{O}^{\text{Dangling}}$  (labeled by  $\text{O}^{\text{D}}$  in green) on surface. c) The energy difference calculated by  $\Delta E_{\text{diff}} = \Delta E_{\text{MO}_4^{\text{B}}} - \Delta E_{\text{MO}_4^{\text{D}}}$  showing the accommodation site preference of each cation, negative (left) for  $\text{MO}_4^{\text{B}}$  energetically preferred while positive (right) for  $\text{MO}_4^{\text{D}}$  energetically preferred. d) The relationship between M-O bond length and ionic radius of studied ions. e) Atomic scheme showing the intercalation of various cations in  $\text{V}_2\text{O}_5$ :  $\text{Na}^+$  cation accommodated by forming the  $\text{MO}_4^{\text{B}}$  bond;  $\text{Mg}^{2+}$  cation accommodated by forming the  $\text{MO}_4^{\text{D}}$  bond;  $\text{NH}_4^+$  cation accommodated by forming the  $\text{MO}_2^{\text{D}}$  bond; and the multiple cation synergistic pillaring effect related with the host of various cations at different accommodation sites.

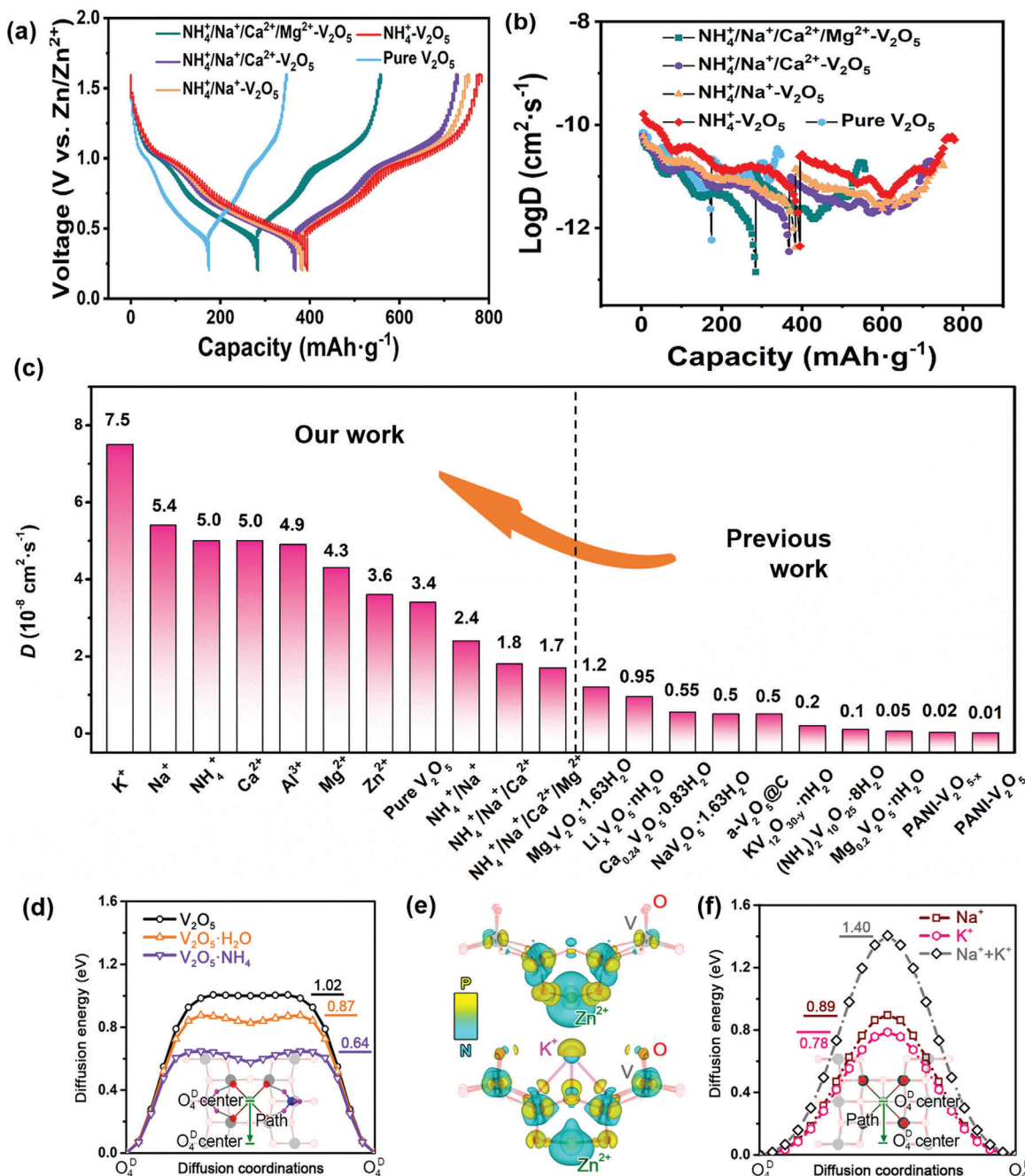


**Figure 5.** a, b) Galvanostatic intermittent titration technique (GITT) analysis of the multiple cation confinement samples by this supramolecular self-assembly. c) Comparison of the Zn<sup>2+</sup> diffusion coefficient in our assemble series and some previous works.<sup>[23–25,43,47–52]</sup> d) Comparison of the energy barriers of the Zn<sup>2+</sup> migration pathways with and without the impacts of H<sub>2</sub>O, NH<sub>4</sub> molecules in large void (LV) space respectively. e) The mapping of charge difference density demonstrating the bonding property between V<sub>2</sub>O<sub>5</sub> and Zn<sup>2+</sup> ion after K<sup>+</sup> confinement. f) Comparison of the energy barriers of the Zn<sup>2+</sup> migration pathways with Na<sup>+</sup>, K<sup>+</sup>, and Na<sup>+</sup>+K<sup>+</sup> confinement, respectively.

diffusion barrier of 1.40 eV, which is remarkably higher than that of unitary Na<sup>+</sup> or K<sup>+</sup> confinement. Accordingly, the nanoconfinement of unitary ions such as K<sup>+</sup>, Na<sup>+</sup>, and NH<sub>4</sub><sup>+</sup> in V<sub>2</sub>O<sub>5</sub> framework promotes the mobility of Zn ion with a much declined Zn<sup>2+</sup> diffusion barrier. However, the further increase in the category of intercalation cation to binary or even quarternary system drastically rise the barrier despite of the expanded interlayer distance.

### 3. Conclusions

We developed a general, supramolecular self-assembly strategy to nanoconfine unitary cation including NH<sub>4</sub><sup>+</sup>, Na<sup>+</sup>, K<sup>+</sup>, Mg<sup>2+</sup>, Ca<sup>2+</sup>, Zn<sup>2+</sup>, Al<sup>3+</sup>, and multiple cations (NH<sub>4</sub><sup>+</sup> + Na<sup>+</sup>, NH<sub>4</sub><sup>+</sup> + Na<sup>+</sup> + Ca<sup>2+</sup>, NH<sub>4</sub><sup>+</sup> + Na<sup>+</sup> + Ca<sup>2+</sup> + Mg<sup>2+</sup>) in ultrathin V<sub>2</sub>O<sub>5</sub> nanosheet. We make a systematic comparison of the Zn<sup>2+</sup> storage

capacity, long-term cycling stability, and Zn-ion diffusion kinetics in this self-assembly series. To this end, there are three results which can be concluded from the present study: (1) For the specific capacity:  $\text{NH}_4^+ > \text{binary} (\text{NH}_4^+ + \text{Na}^+) > \text{ternary} (\text{NH}_4^+ + \text{Na}^+ + \text{Ca}^{2+}) > \text{Na}^+ > \text{Ca}^{2+} > \text{Mg}^{2+} > \text{quaternary} (\text{NH}_4^+ + \text{Na}^+ + \text{Ca}^{2+} + \text{Mg}^{2+}) > \text{Zn}^{2+} > \text{Al}^{3+} > \text{bare } \text{V}_2\text{O}_5$ ; (2) for the capacity retention after long-term cycling:  $R_{\text{quaternary}} > R_{\text{ternary}} > R_{\text{binary}}$ ; (3) for the  $\text{Zn}^{2+}$  diffusion coefficient:  $D_{\text{K}^+} > D_{\text{Na}^+} > D_{\text{NH}_4^+} > D_{\text{Ca}^{2+}} > D_{\text{Al}^{3+}} > D_{\text{Mg}^{2+}} > D_{\text{Zn}^{2+}} > D_{\text{bare } \text{V}_2\text{O}_5} > D_{\text{binary}} > D_{\text{ternary}} > D_{\text{quaternary}}$ . The unitary cation confinement enables a remarkable increase in the  $\text{Zn}^{2+}$  storage capacity and diffusion kinetics, and the multiple cation confinement gives rise to superior long-term cyclability and structural stability due to multiple cation synergetic pillaring effect. DFT simulation further reveals a declined Zn-ion diffusion barrier by unitary cation nanoconfinement due to a significantly weakened interaction between  $\text{Zn}^{2+}$  and the dangling oxygen atom of  $\text{V}_2\text{O}_5$ . Our work develops a novel multiple cations nanoconfinement strategy toward high-performance cathode for aqueous battery, and it also provides new insight into the guest cation regulation of zinc-ion diffusion kinetics and long-term cyclability. Such a supramolecular self-assembly strategy could be extended to the high-entropy materials preparation due to it is facile to introduce various metallic cations into the host frameworks.

## 4. Experimental Section

**Supramolecular Self-Assembly:** All chemical reagents were used without any purification. In a typical preparation process, 0.3638 g  $\text{V}_2\text{O}_5$  (99.99%, Sigma Aldrich) was dissolved into 27 mL deionized water. After the addition of 8 mL  $\text{H}_2\text{O}_2$  (30wt%, Aladdin), the mixture was stirred for 90 min until a clear claret-red solution was achieved. The above homogeneous solution was then transferred into a 50 mL Teflon-lined stainless-steel autoclave and hydrothermally treated at 200 °C for 48 h to acquire orange colloid consisted of  $\text{V}_2\text{O}_5$  nanosheets. Subsequently, the obtained orange  $\text{V}_2\text{O}_5$  nanosheet colloid was diluted by deionized water and added dropwise to 0.2 mol  $\text{L}^{-1}$   $\text{MCl}_x$  (M refers to  $\text{Na}^+$ ,  $\text{K}^+$ ,  $\text{Mg}^{2+}$ ,  $\text{Ca}^{2+}$ ,  $\text{Zn}^{2+}$ ,  $\text{Al}^{3+}$ ,  $\text{NH}_4^+$ ) solution to realize the colloidal self-assembly procedure along with stirring. The single self-assembly flocculation product was collected after stirring several hours and washed with deionized water for three times. The final product was achieved after drying in vacuum oven at 80 °C for 24 h. Cooperative self-assembly was realized by the similar procedure with the dropwise addition of a mixture salt solution ( $\text{NH}_4\text{Cl} + \text{NaCl}$ ;  $\text{NH}_4\text{Cl} + \text{NaCl} + \text{MgCl}_2$ ;  $\text{NH}_4\text{Cl} + \text{NaCl} + \text{MgCl}_2 + \text{CaCl}_2$ , respectively. 0.2 mol  $\text{L}^{-1}$  for each cation in the solution) into the  $\text{V}_2\text{O}_5$  nanosheet colloid.

As a contrast experiment using the conventional hydrothermal route, 0.2 g of  $\text{V}_2\text{O}_5$  was added to  $\text{C}_2\text{H}_5\text{OH}$  and stirred until the solution was evenly dispersed, which was designated as solution B. An amount of 0.03 g  $\text{NH}_4\text{Cl}$ , 0.03 g  $\text{NaCl}$ , 0.03 g  $\text{CaCl}_2$ , and 0.03 g  $\text{MgCl}_2$  were dissolved in deionized water (the volume ratio of ethanol: deionized water was 5:4) to obtain solution C. Then solution C was added to solution B, stirred vigorously until the solution was uniformly dispersed. The mixed solution was transferred to a 50 mL autoclave, sealed, and kept at 160 °C for 24 h. After cooling to room temperature, the product was recovered through centrifugation and washed several times with DI water and ethanol.

**Materials Characterization:** The crystal structure characteristics were studied by Ultima IV diffractometer which used  $\text{Cu } K\alpha$  radiation ( $\lambda = 1.5406 \text{ \AA}$ ). TGA measurements were carried out using a TG203 F3 instrument in a temperature range of 25 °C to 600 °C at a heating rate of 5 °C  $\text{min}^{-1}$  under nitrogen atmosphere. SEM images were generated by FEI 3D field emission scanning electron microscope. TEM, SAED, and mapping

were performed using jem:2100f field emission transmission electron microscope. ICP emission spectrometer was using Agilent 5100 to evaluate metal element ratios. Escalab 250Xi X-ray photoelectron spectroscopy system (XPS) was devoted into service for the analysis of element chemical state of the samples, with a  $\text{C}1s$  peak at 284.8 eV as the standard signal. Layered morphology was investigated by using Shimadzu spm-9700 atomic force microscope. Fourier-transform infrared (FT-IR) and Raman spectroscopies were performed using Bruker TENSOR II infrared spectrometer to analyze and LabRAM HR Evolution spectrometer, respectively.

**Electrochemical Measurement:** The as-prepared  $\text{M}_x\text{V}_2\text{O}_5 \cdot n\text{H}_2\text{O}$  materials, conductive carbon and polyvinylidene fluoride (PVDF) were mixed at a weight ratio of 7:2:1 with *N*-methylpyrrolidone (NMP) as a solution to make a homogeneous slurry. It was pasted onto stainless steel slice and dried in vacuum atmosphere at 60 °C. The cells were assembled with the as-prepared materials as cathode, zinc foils as anode, Whatman GF/D glass fibers as separator, and 2.0 M  $\text{Zn}(\text{OTf})_2$  aqueous solution (Alfa) as electrolyte. The CV tests and EIS were studied on the electrochemical workstation CHI660E. GCD was tested on a LANDdt battery tester system (China). GITT was applied to investigate the diffusion kinetics for  $\text{Zn}^{2+}$  in different  $\text{M}_x\text{V}_2\text{O}_5 \cdot n\text{H}_2\text{O}$ .

**Calculation Method:** The modeling in this work was performed in the framework of DFT as implemented in the Vienna Ab initio Simulation Package (VASP). The Projector Augmented Wave (PAW) method was adopted to solve the Kohn–Sham equations, and the generalized gradient approximation constructed by Perdew–Burke–Ernzerhof (GGA–PBE) was taken for exchange–correlation functional. All the investigated structures in this work were fully relaxed at the cutoff energy of 480 eV in a  $\Gamma$ -centered *k*-grid scheme with a total number of 40, during which process the convergence criteria were set to be  $10^{-4}$  eV for energy and  $10^{-2}$  eV  $\text{\AA}^{-1}$  for force. The monolayer  $\text{V}_2\text{O}_5$  was constructed based on the optimized bulk  $\text{V}_2\text{O}_5$ , by setting a lattice parameter *c* of 11.0 Å according to the XRD characterization results. Thereafter, the intercalation/absorption of ions (Na, Mg, Al, K, Ca, and Zn) and molecules ( $\text{H}_2\text{O}$  and  $\text{NH}_4$ ) on the  $\text{V}_2\text{O}_5$  monolayer was investigated by computing the formation energy, and the accommodation site preference of each cation was then revealed by calculating the energy difference, according to  $\Delta E_{\text{diff}} = \Delta E_{\text{MO}_4^{\text{B}}} - \Delta E_{\text{MO}_4^{\text{D}}}$ , in which  $\Delta E_{\text{MO}_4^{\text{B}}}$  refers to the intercalation energy of M cation on  $\text{V}_2\text{O}_5$  while forming  $\text{MO}_4^{\text{B}}$  bonds, and  $\Delta E_{\text{MO}_4^{\text{D}}}$  refers to the intercalation energy of M cation on  $\text{V}_2\text{O}_5$  while forming  $\text{MO}_4^{\text{D}}$  bonds.

## Supporting Information

Supporting Information is available from the Wiley Online Library or from the author.

## Acknowledgements

Y.L. and C.J.L. contributed equally to this work. This work was financially supported by the National Key Research and Development Program of China (Grant No. 2021YFB2400400), the National Natural Science Foundation of China (52171203, 52371214, 52101261, 52302224 and 52131306), the Natural Science Foundation of Jiangsu Province (Grant No. BK20211516 and BK20221179), the Jiangsu Province Excellent Post-Doctoral Program (2022ZB77), and the Fundamental Research Funds for the Central Universities (2242023K5001).

## Conflict of Interest

The authors declare no conflict of interest.

## Data Availability Statement

Research data are not shared.

## Keywords

aqueous zinc-ion battery, ion diffusion kinetic, multiple cations, nanoconfinement, supramolecular assembly

Received: December 1, 2023  
Published online: January 29, 2024

- [1] R. F. Service, *Science*. **2021**, 372, 890.
- [2] Y. L. Liang, H. Dong, D. Aurbach, Y. Yao, *Nat. Energy*. **2020**, 5, 646.
- [3] J. Kim, Y. Park, M. Kim, J. Lee, K. J. Kim, J. W. Choi, *Nat. Commun.* **2022**, 13, 2371.
- [4] Z. D. Zhao, R. Wang, C. X. Peng, W. J. Chen, T. Q. Wu, B. Hu, W. J. Weng, Y. Yao, J. X. Zeng, Z. H. Chen, P. Y. Liu, Y. C. Liu, G. S. Li, J. Guo, H. B. Lu, Z. P. Guo, *Nat. Commun.* **2021**, 12, 6606.
- [5] S. Jin, Y. Q. Shao, X. S. Gao, P. Y. Chen, J. X. Zheng, S. F. Hong, J. F. Yin, Y. L. Joo, L. A. Archer, *Sci. Adv.* **2022**, 8, 4456.
- [6] L. Ma, M. A. Schroeder, O. Borodin, T. P. Pollard, M. S. Ding, C. S. Wang, K. Xu, *Nat. Energy*. **2022**, 5, 743.
- [7] L. L. Wang, K. W. Huang, J. T. Chen, J. R. Zheng, *Sci. Adv.* **2019**, 5, 4279.
- [8] H. B. Dong, J. W. Li, J. Guo, F. L. Lai, F. J. Zhao, Y. D. Jiao, D. J. L. Brett, T. X. Liu, G. J. He, L. P. Parkin, *Adv. Mater.* **2021**, 33, 2007548.
- [9] Y. Liu, J. Wang, Y. X. Zeng, J. Liu, X. Q. Liu, X. H. Lu, *Small*. **2020**, 16, 1907458.
- [10] H. F. Liang, Z. Cao, F. W. Ming, W. L. Zhang, D. H. Anjum, Y. Cui, L. Cavallo, H. N. Alshareef, *Nano Lett.* **2019**, 19, 3199.
- [11] W. S. V. Lee, T. Xiong, X. P. Wang, J. M. Xue, *Small Methods*. **2021**, 5, 2000815.
- [12] H. L. Pan, Y. Y. Shao, P. F. Yan, Y. W. Cheng, K. S. Han, Z. M. Nie, C. M. Wang, J. H. Yang, X. L. Li, P. Bhattacharya, K. T. Mueller, J. Liu, *Nat. Energy*. **2016**, 1, 16039.
- [13] X. L. Zhou, K. X. Ma, Q. Y. Zhang, G. Z. Yang, C. X. Wang, *Nano Res.* **2022**, 15, 8039.
- [14] S. S. Zhang, Z. J. Liu, L. Li, S. K. Li, S. Q. Zhang, Y. D. Tang, J. L. Yu, H. Y. Zhang, *Chem. Commun.* **2021**, 57, 10339.
- [15] L. T. Ma, S. M. Chen, C. B. Long, X. L. Li, Y. W. Zhao, Z. X. Liu, Z. D. Huang, B. B. Dong, J. A. Zapien, C. Y. Zhi, *Adv. Energy Mater.* **2019**, 9, 1902446.
- [16] S. Islam, M. H. Alfaruqi, V. Mathew, J. J. Song, S. J. Kim, S. Kim, J. Jo, J. P. Baboo, D. T. Pham, D. Y. Putro, Y. K. Sun, J. K. Kim, *J. Mater. Chem. A*. **2017**, 5, 23299.
- [17] M. H. Alfaruqi, V. Mathew, J. Gim, S. J. Kim, J. J. Song, J. P. Baboo, S. H. Choi, J. Kim, *Chem. Mater.* **2015**, 27, 3609.
- [18] B. K. Wu, G. B. Zhang, M. Y. Yan, T. F. Xiong, P. He, L. He, X. Xu, L. Q. Mai, *Small*. **2018**, 14, 1703850.
- [19] Z. Liu, G. Pulletikurthi, F. Endres, *ACS Appl. Mater. Interfaces*. **2016**, 8, 12158.
- [20] R. Trocoli, F. L. Mantia, *ChemSusChem*. **2015**, 8, 481.
- [21] L. Y. Zhang, L. Chen, X. F. Zhou, Z. P. Liu, *Adv. Energy Mater.* **2015**, 5, 1400930.
- [22] R. F. Service, *Science*. **2018**, 362, 508.
- [23] S. C. Liu, H. Zhu, B. H. Zhang, G. Li, H. K. Zhu, Y. Ren, H. B. Geng, Y. Yang, Q. Liu, C. C. Li, *Adv. Mater.* **2020**, 32, 2001113.
- [24] W. J. Li, C. Han, Q. F. Gu, S. L. Chou, J. Z. Wang, H. K. Liu, S. X. Dou, *Adv. Energy Mater.* **2020**, 10, 2001852.
- [25] Y. Q. Yang, Y. Tang, G. Z. Fang, L. T. Shan, J. S. Guo, W. Y. Zhang, C. Wang, L. B. Wang, J. Zhou, S. Q. Liang, *Environ. Sci.* **2018**, 11, 3157.
- [26] C. Xia, J. Guo, P. Li, X. X. Zhang, H. N. Alshareef, *Angew. Chem., Int. Ed.* **2018**, 57, 4007.
- [27] T. T. Lv, G. Y. Zhu, S. Y. Dong, Q. Q. Kong, Y. Peng, S. Jiang, G. X. Zhang, Z. L. Yang, S. Y. Yang, X. C. Dong, H. Pang, Y. Z. Zhang, *Angew. Chem., Int. Ed.* **2023**, 62, 202216089.
- [28] L. F. Hu, Z. Y. Wu, C. J. Lu, F. Ye, Q. Liu, Z. M. Sun, *Environ. Sci.* **2021**, 14, 4095.
- [29] R. Li, F. Xing, T. Y. Li, H. M. Zhang, J. W. Yan, Q. Zheng, X. F. Li, *Energy Storage Mater.* **2021**, 38, 590.
- [30] L. Z. Wang, K. Takada, A. Kajiyama, M. Onoda, Y. Michiue, L. Q. Zhang, M. Watanabe, T. Sasaki, *Chem. Mater.* **2003**, 15, 4508.
- [31] R. Z. Ma, X. H. Liu, J. B. Liang, Y. Bando, T. Sasaki, *Adv. Mater.* **2014**, 26, 4173.
- [32] P. Xiong, B. Sun, N. Sakai, R. Z. Ma, T. Sasaki, S. J. Wang, J. Q. Zhang, G. X. Wang, *Adv. Mater.* **2020**, 32, 1902654.
- [33] S. Y. Dong, W. Shin, H. Jiang, X. Y. Wu, Z. F. Li, J. Holoubek, W. F. Stickle, B. Key, C. Liu, J. Lu, P. A. Greaney, X. G. Zhang, X. L. Ji, *Chem.* **2019**, 5, 1537.
- [34] T. Sasaki, M. Watanabe, H. Hashizume, H. Yamada, H. Nakazawa, *Am. Chem. Soc.* **1996**, 118, 8329.
- [35] X. Lu, Y. Zhang, J. Zheng, H. Jiang, T. Hu, C. G. Meng, *J. Am. Chem. Soc.* **2007**, 129, 8000.
- [36] C. C. Torardi, C. R. Miao, M. E. Lewittes, Z. Li, *Angew. Chem., Int. Ed.* **2019**, 58, 7062.
- [37] Z. P. Liu, R. Z. Ma, M. Osada, K. Takada, T. Sasaki, *J. Am. Chem. Soc.* **2005**, 127, 13869.
- [38] N. Lv, R. Q. Ren, Y. L. Wu, Z. K. Xu, D. X. Wu, X. Y. You, G. Y. Zhu, Y. Z. Zhang, S. Y. Dong, *Electrochim. Acta*. **2022**, 431, 141097.
- [39] Y. Gogotsi, R. M. Penner, *ACS Nano*. **2018**, 12, 2081.
- [40] V. Augustyn, J. Come, M. A. Lowe, J. W. Kim, P. L. Taberna, S. H. Tolbert, H. D. Abruna, P. Simon, B. Dunn, *Nat. Mater.* **2013**, 12, 518.
- [41] X. Liu, H. Zheng, D. Geiger, J. Han, A. Varzi, U. Kaiser, A. Moretti, S. Passerini, *Chem. Commun.* **2019**, 55, 2265.
- [42] W. J. Zhou, J. Z. Chen, M. F. Chen, A. R. Wang, A. X. Huang, X. W. Xu, J. L. Xu, C. P. Wong, *J. Mater. Chem.* **2020**, A 8, 8397.
- [43] P. Hu, T. Zhu, X. P. Wang, X. J. Wei, M. Y. Yan, J. T. Li, W. Luo, W. C. Zhang, L. Zhou, Z. Q. Zhou, L. Q. Mai, *Nano Lett.* **2018**, 18, 1758.
- [44] Y. Q. Fan, Z. X. Qu, W. T. Zhong, Z. W. Hu, H. A. Younus, C. H. Yang, X. W. Wang, S. G. Zhang, *ACS Appl. Mater. Interfaces*. **2021**, 13, 7377.
- [45] P. He, M. Y. Yan, X. B. Liao, Y. Z. Luo, L. Q. Mai, C. W. Nan, *J. Mater. Chem. A*. **2019**, 7, 20806.
- [46] B. Y. Tang, L. T. Shan, S. Q. Liang, J. Zhou, *Energy Environ. Sci.* **2019**, 12, 3288.
- [47] T. Meng, C. F. Liu, J. Q. Zheng, X. X. Jia, E. P. Jahrman, G. T. Seidler, D. H. Long, M. Atif, M. Alsalhi, G. Z. Cao, *Energy Storage Mater.* **2020**, 29, 9.
- [48] F. W. Ming, H. F. Liang, Y. J. Lei, S. Kandambeth, M. Eddaoudi, H. N. Alshareef, *ACS Energy Lett.* **2018**, 3, 2602.
- [49] C. Xia, J. Guo, P. Li, X. X. Zhang, H. N. Alshareef, *Angew. Chem., Int. Ed.* **2018**, 57, 3943.
- [50] S. Z. Deng, Z. S. Yuan, Z. W. Tie, C. D. Wang, L. Song, Z. Q. Niu, *Angew. Chem., Int. Ed.* **2020**, 59, 22002.
- [51] T. Y. Wei, Q. Li, G. Z. Yang, C. X. Wang, *J. Mater. Chem. A*. **2018**, 6, 20402.
- [52] J. D. Guan, L. Y. Shao, L. Yu, S. G. Wang, X. Y. Shi, J. J. Cai, Z. P. Sun, *Chem. Eng. J.* **2022**, 443, 136502.
- [53] G. X. Liu, H. W. Huang, R. Bi, X. Xiao, T. Y. Ma, L. Zhang, *Adv. Energy Mater.* **2023**, 13, 2202515.